Joule

CellPress

Article

A microchanneled solid electrolyte for carbon-efficient CO_2 electrolysis

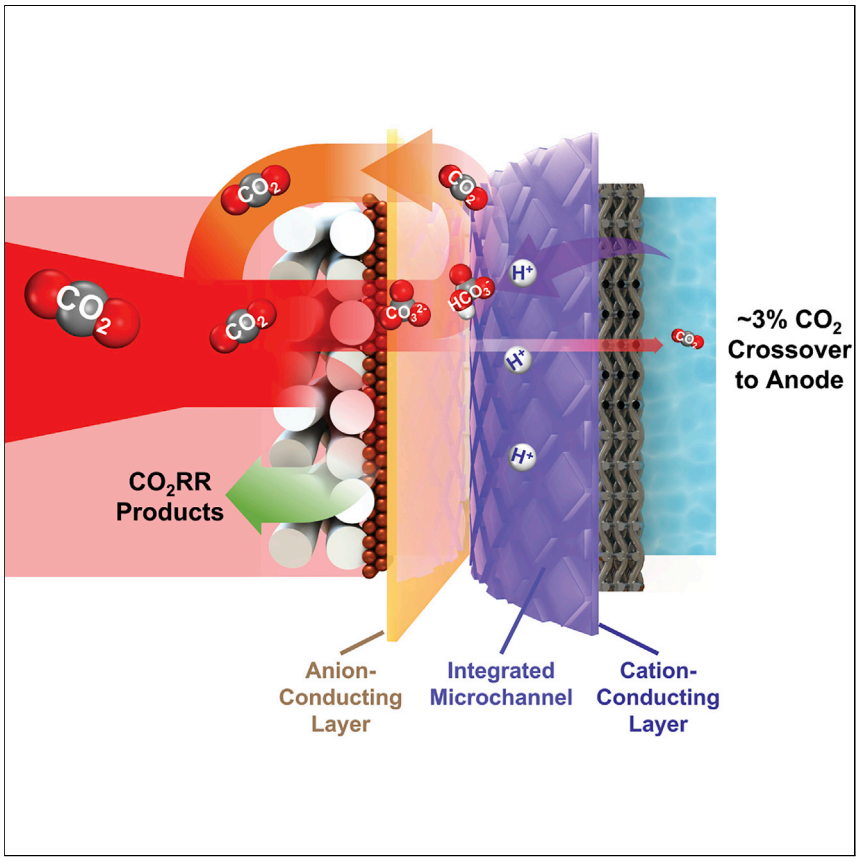

CO_2 electrolysis is a promising technology that can utilize intermittent renewable electricity to mitigate CO_2 emissions. In conventional electrolyzers, most of the reactant CO_2 is lost to parasitic side reactions, limiting the electrochemical conversion of CO_2 into valuable products. Here, we present a microchanneled solid electrolyte that internally regenerates and recycles CO_2, thereby eliminating CO_2 loss. Implementing fixed cations in place of traditional alkali metal cations enables stable and selective CO_2 electrolysis to multi-carbon products.

Yi Xu, Rui Kai Miao, Jonathan P. Edwards, ..., Anthony Robb, Edward H. Sargent, David Sinton

sinton@mie.utoronto.ca

Highlights

MSE reduces CO_2RR reactant loss to near-zero (~3%)

Fixed cations in the MSE enable alkali metal cation free operation

Selective multi-carbon production (77%) at industrially relevant current densities

Stable continuous electrolysis for >200 h at a current density of 100 mA cm^{-2}

Xu et al., Joule 6, 1–11
June 15, 2022
https://doi.org/10.1016/j.joule.2022.04.023

Please cite this article in press as: Xu et al., A microchanneled solid electrolyte for carbon-efficient CO_2 electrolysis, Joule (2022), https://doi.org/10.1016/j.joule.2022.04.023

Joule

CellPress

Article

A microchanneled solid electrolyte for carbon-efficient CO_2 electrolysis

Yi Xu,[1,3] Rui Kai Miao,[1,3] Jonathan P. Edwards,[1,3] Shijie Liu,[1] Colin P. O'Brien,[1] Christine M. Gabardo,[1] Mengyang Fan,[1] Jianan Erick Huang,[2] Anthony Robb,[1] Edward H. Sargent,[2] and David Sinton[1,4,*]

SUMMARY

The electrochemical reduction of CO_2 is a promising route to convert carbon emissions into valuable chemicals and fuels. In electrolyzers producing multi-carbon products, 70%–95% of the supplied CO_2 is converted to (bi)carbonates, limiting the carbon efficiency of electrochemical CO_2 conversion. These (bi)carbonate anions can be lost to the aqueous electrolyte, converted back to gaseous CO_2 and diluted in the anode tail gas, and/or combined with alkali metal cations from the electrolyte to form solid salt precipitates. Here, we report a microchanneled solid electrolyte that allows for the recapture and recycling of (bi)carbonate ions before reaching the anode, reducing CO_2 loss to ~3%. We demonstrate CO_2 electroreduction to multi-carbon products with 77% selectivity without the use of alkali metal cations, by incorporating fixed quaternary ammonium cations. This system simultaneously achieves near-zero CO_2 loss, high selectivity toward multi-carbon products, and stable operation at an industrially relevant current density over 200 h.

INTRODUCTION

The electrochemical carbon dioxide reduction reaction (CO_2RR) enables utilization of intermittent renewable electricity and the mitigation of CO_2 emissions.[1–3] Copper-based CO_2RR catalysts generate valuable multi-carbon chemicals (C_{2+}) at industrially relevant reaction rates and selectivities.[4–10] Performing CO_2RR at industrially relevant reaction rates generates alkaline conditions that are favorable for CO_2RR but promote the rapid chemical conversion of CO_2 to (bi)carbonates.[11,12] In C_{2+} electrolyzers, 70%–95% of the supplied CO_2 is converted to (bi)carbonates and is lost to the electrolyte,[13–15] anode tail gas,[16–18] and cathode salt precipitation[19–21] (Figure 1A). A small fraction of the remaining CO_2 is converted to products in conventional systems (supplemental information section 1).[7,13–17,22]

Recovering lost CO_2 reactant incurs an economic penalty 0.7–5 times the ethylene (C_2H_4) market price (see supplemental information section 2).[13] In addition to trapping CO_2, the accumulation of salt within the system limits CO_2RR performance and stability.[19,20,23–25] The loss of CO_2 can be reduced by employing bipolar membranes[26–28] and solid-state electrolyte packed beds[29–33] and by surrounding the locally alkaline cathode with acidic electrolyte that regenerates gaseous CO_2 (Huang et al.[34]); however, none of these approaches has produced C_{2+} with high stability (>12 h) and energy efficiency (EE, ~14%).[34] Eliminating alkali metal cations could avoid salt precipitation, but these are viewed as essential for efficient CO_2RR.[21,34]

Here, we report a microchanneled solid electrolyte (MSE), enabling net carbon-efficient CO_2 electrolysis. By exploiting the pH swing caused by CO_2 electrolysis, we internally

Context & scale

CO_2 electrolysis is a promising technology to convert carbon emissions into valuable chemicals and fuels. In conventional CO_2 electrolyzers, the majority of the reactant CO_2 is lost to (bi)carbonate formation, limiting the carbon efficiency of electrochemical CO_2 conversion. Here, we report a microchanneled solid electrolyte that allows for the internal recapture and recycle of (bi)carbonate ions before they are lost to the anode, drastically reducing the CO_2 loss. By incorporating fixed quaternary ammonium cations, we demonstrate CO_2 electroreduction to multi-carbon products without the use of alkali metal cations, the latter of which cause destructive salt precipitation. This system simultaneously achieves near-zero CO_2 loss, high selectivity toward multi-carbon products, and stable operation at an industrially relevant current density.

Please cite this article in press as: Xu et al., A microchanneled solid electrolyte for carbon-efficient CO_2 electrolysis, Joule (2022), https://doi.org/10.1016/j.joule.2022.04.023

regenerate high purity CO_2 (98% v/v) from (bi)carbonate ions, the latter of which causes CO_2 loss to anode tail gas and electrolyte. To prevent CO_2 loss to the salt formation while facilitating efficient CO_2RR, we employ fixed quaternary ammonium cations from poly(aryl piperidinium) instead of relying on mobile alkali metal cations in aqueous electrolytes. We report, as a result, peak C_2H_4 selectivity of 51% with only ~3% CO_2 loss. We achieve over 200 h of stable operation without signs of performance degradation. The C_{2+} EE is 27% at 100 mA cm^{-2}, comparable with the best reported CO_2 electrolyzers, yet with more than 20 times lower CO_2 loss.[7–9]

RESULTS AND DISCUSSION

Internal capture to eliminate CO_2 crossover

To better understand CO_2 crossover within conventional anion-conducting solid electrolytes (Figure 1B), we began with numerical multi-physics simulations (supplemental information section 3). The anodic oxygen (O_2) evolution reaction makes the anode locally acidic and shifts the (bi)carbonate equilibria toward dissolved gaseous CO_2. The dissolved CO_2 then exceeds the solubility limit in the liquid anolyte and gaseous CO_2 comes out of the solution, mixing with the generated O_2 (Figures 1C and S1).[16,18] Noting that it is the blending of CO_2 with anode-produced O_2 that results in costly downstream separation,[35] we postulated that capturing CO_2 en route to the anode—desorbing CO_2 in the absence of O_2—would enable direct recycling of the reactant in pure form while eliminating two primary sources of CO_2 loss: the anode tail gas and electrolyte.

To test this hypothesis, we sought to develop an MSE, wherein (bi)carbonate ions encounter acidic conditions and the regenerated CO_2 could be captured and recirculated to the cathode (Figure 1D). We envisioned integrated channels within a cation-conducting layer for CO_2 capture, assembled into a zero-gap electrolyzer configuration. The anion-conducting layer would achieve high pH conditions at the cathode favorable for CO_2RR and the cation-conducting layer would provide proton transport and an acidic pH for internal CO_2 regeneration (<4 pH).[36] We modeled the transport of (bi)carbonates and protons to the internal CO_2 regeneration domain at the interface of the anion- and cation-conducting layers. The simulations indicate that under operating conditions, the integrated channel layer would be sufficiently acidic to transform incoming (bi)carbonates to CO_2, exceeding the solubility limit and causing gas-phase CO_2 evolution (Figures 1E and S2).

To test internal CO_2 regeneration experimentally, we created a pH-swing CO_2 capture domain at the interface of anion- and cation-conducting layers with integrated channels for CO_2 extraction. Structuring the channels in the cation-conducting layer was preferable due to the better mechanical and thermal durability, and the higher conductivity when compared to the anion-conducting layer. The assembly was integrated into a zero-gap CO_2 electrolyzer making use of a copper catalyst on the cathode and iridium oxide catalyst on the anode. When we operated the system at current densities ranging from 40 to 240 mA cm^{-2}, the composition of the gas leaving the integrated channels was constant at 98% v/v CO_2 (Figure 1F; Table S1A). Also present were traces of hydrogen (H_2) and O_2, owing to diffusion from the cathode and anode, respectively. Analysis of the anodic tail gas indicated a CO_2 concentration of ~7% v/v, independent of current density (Figure 1G; Table S1A). This fraction of CO_2 diffuses to the anode in dissolved form, due to concentration gradients between the interface and the anode.[37] Based on the measured stream compositions, we quantified all CO_2 pathways (electroreduced, internally regenerated/recirculated, and released at the anode) over the range of current densities (Figure 1H; Table S1B; supplemental information section 4). In all cases, the

[1]Department of Mechanical and Industrial Engineering, University of Toronto, 5 King's College Road, Toronto, ON M5S 3G8, Canada

[2]Department of Electrical and Computer Engineering, University of Toronto, 10 King's College Road, Toronto, ON M5S 3G4, Canada

[3]These authors contributed equally

[4]Lead contact

*Correspondence: sinton@mie.utoronto.ca

https://doi.org/10.1016/j.joule.2022.04.023

Please cite this article in press as: Xu et al., A microchanneled solid electrolyte for carbon-efficient CO_2 electrolysis, Joule (2022), https://doi.org/10.1016/j.joule.2022.04.023

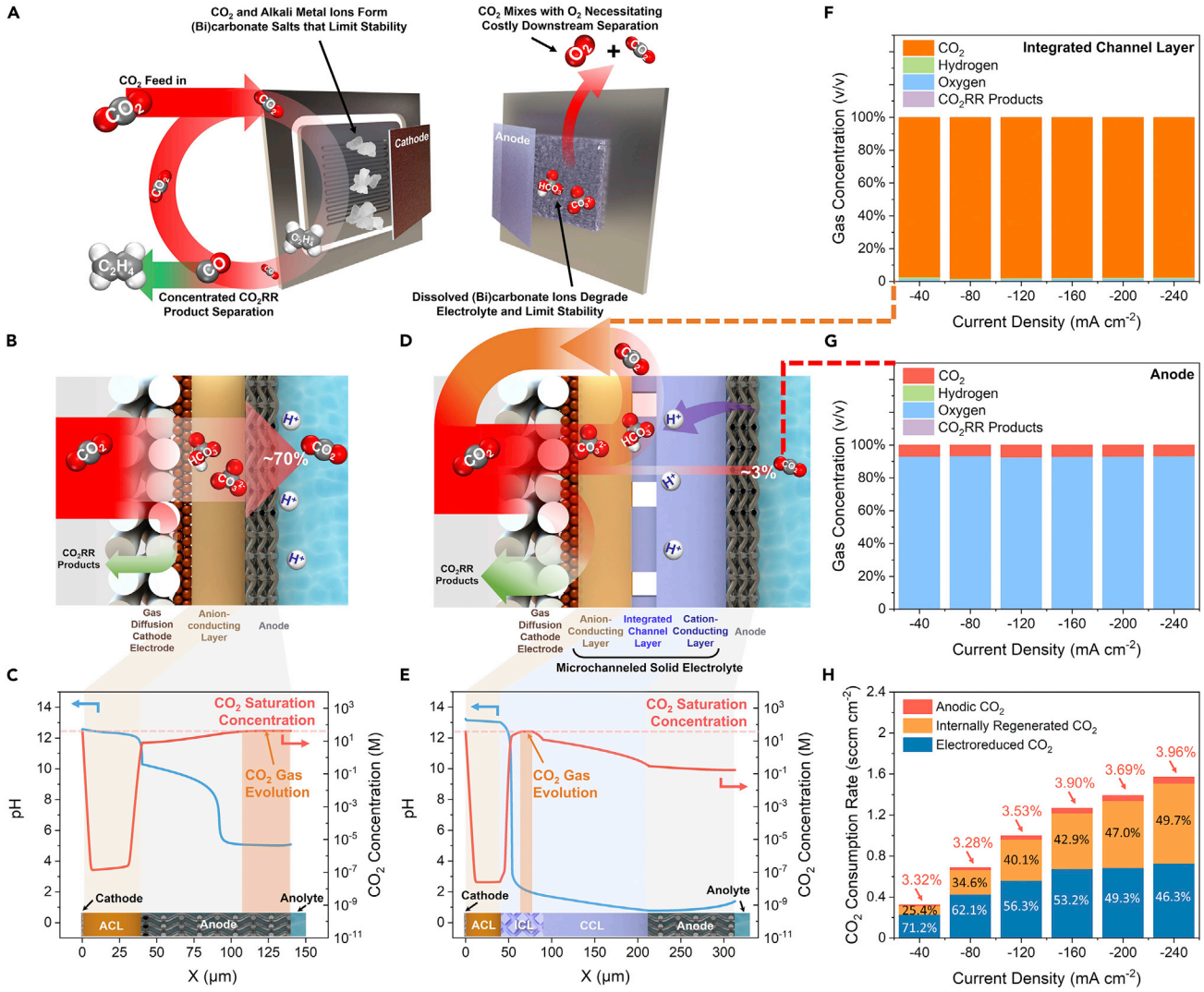

Figure 1. CO_2RR with near-zero CO_2 loss

(A) Schematic showing the sources of CO_2 loss and instability in conventional electrolyzers with anion-conducting solid electrolytes; CO_2 loss to (bi) carbonates results in salt formation that reduces stability, and gaseous CO_2 evolution at the anode results in a mixture from which CO_2 is costly to separate.

(B) Cross-sectional schematic of (bi)carbonate formation and anodic CO_2 loss with an anion-conducting solid electrolyte.

(C) COMSOL simulation of the dissolved CO_2 concentration and pH distribution with an anion-conducting solid electrolyte (0.1 M $KHCO_3$ anolyte).

(D) Schematic of (bi)carbonate formation and CO_2 recycling with a microchanneled solid electrolyte (MSE) for internal CO_2 regeneration.

(E) COMSOL simulation of the dissolved CO_2 concentration and pH distribution with an MSE for internal CO_2 regeneration.

(F) Composition of the gas collected from the integrated channel layer.

(G and H) (G) Composition of the gas collected from the anode, and (H) CO_2 consumption rate.

The experimental data collected in (F), (G), and (H) were collected with a CO_2 feed rate of 20 sccm cm^{-2} into the electrolyzer and 0.01 M H_2SO_4 anolyte. The error for (F), (G), and (H) is indicated in Table S1.

fraction of CO_2 converted (chemically and electrochemically) in the reactor that is lost to the anode tail gas is between 3% and 4%.

Design of MSE geometry

The integrated channel layer within the MSE needs to facilitate efficient mass and ion transfer in parallel, allowing for water transport, ion transport, and gaseous CO_2 evolution and collection (Figure 2A). The hydraulic diameter and interconnectedness of

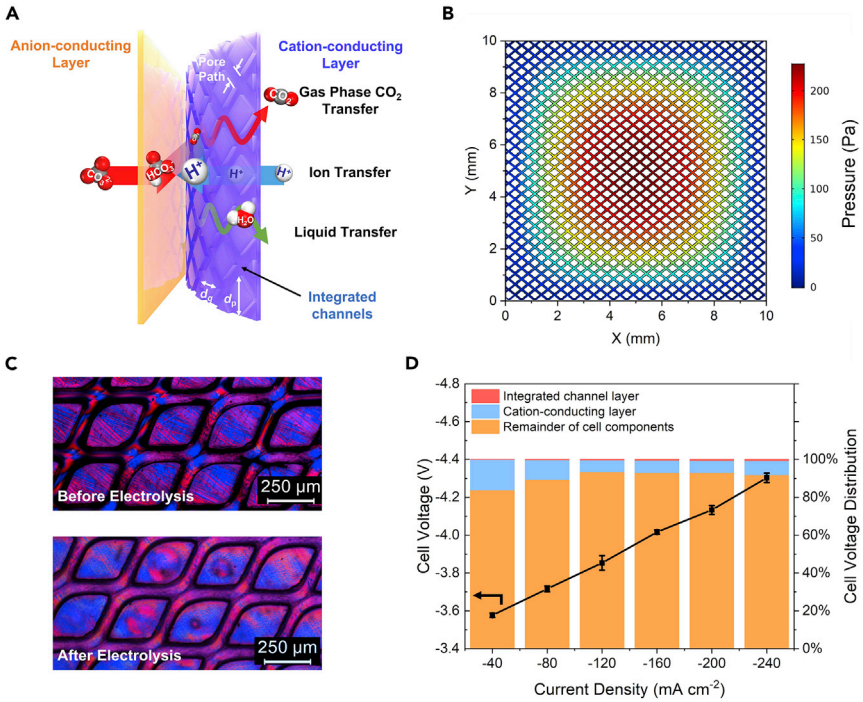

Figure 2. Design of microchanneled solid electrolyte for internal CO_2 regeneration

(A) Schematic demonstrating the parallel flows of gas-phase CO_2, liquids, and ions.

(B) COMSOL simulation of the maximum channel pressure induced by the creation and flow of internally captured CO_2 for a pore path size of 75 μm (1 cm^2, 100 mA cm^{-2}). The maximum pressure distribution of other pore path sizes is shown in Table S2.

(C) Integrated channel layer before and after electrolysis (total electrolyzer geometric area: 1 cm^2).

(D) Experimental cell voltages of the electrolyzer with the microchanneled solid electrolyte (0.01 M H_2SO_4 anolyte) and cell voltage distribution. The methodology for determining the voltage distribution is indicated in supplemental information section 6. Error bars represent the standard deviation of the voltage in three independent experiments.

the channels influence CO_2 removal, internal pressure build-up, and stability. The porosity of the layer influences ion transfer, ohmic losses, and EE. This coupled design challenge has been addressed by natural systems—leaves transport water, ions, and gaseous CO_2 through a series of microporous media[38–40]—and the diamond pattern[41,42] exhibits higher permeability than other microstructures of similar porosity (Figure S3).[43] Drawing inspiration from these natural systems, we fabricated an interconnected channel pattern (diamond pillars, d_p = 350 μm, d_q = 250 μm) in the cation-conducting layer via soft lithography and hot embossing. We analyzed the mass transfer resistance of a channel pore path size between 25 and 150 μm using computational fluid dynamics modeling (Figure S4; supplemental information section 5): Pore paths over 75 μm resulted in acceptably low two-phase flow resistance and internal pressures: 0.23 kPa for a 1 cm^2 area (Figure 2B) and 44.1 kPa for an industrial-scale 100 cm^2 area (Table S2). Simulations of internal CO_2 regeneration in the limiting case of a large-area liquid-filled layer, resulted in maximum pressures well below the yield strength of commercial solid anion-conducting layers.[37,44] Smaller microchannels led to repeated cycles of pressure build-up and release. These pressure oscillations are visible on the voltage response and could hamper long-term electrolyzer operation (Figure S5). There was no detectable change in the integrated channel layer, before and after CO_2 electrolysis (Figures 2C and S6). In addition to the active area,[45] another consideration in the

Please cite this article in press as: Xu et al., A microchanneled solid electrolyte for carbon-efficient CO_2 electrolysis, Joule (2022), https://doi.org/10.1016/j.joule.2022.04.023

design of the microchannel network is the current density. At higher current density operation, more CO_2 and water will need to be removed by the integrated microchannels, and thus, the MSE could be designed with larger pores (e.g., >75 μm), and/or a nonuniform network to accommodate larger fluxes within the microchannels.

We operated the electrolyzer with the MSE at cell voltages of −3.6 and −4.3 V to reach current densities of 40 and 240 mA cm^{-2}, respectively (Figure 2D). The MSE had comparable cell voltages (e.g., within 100 mV at current densities >120 mA cm^{-2}) with conventional anion-conducting solid electrolytes with near-neutral anolytes, but with much lower anodic CO_2 loss (Figure S7A). Removing the cation-conducting layer with integrated channels from the MSE lowered the cell voltage but substantially increased CO_2 loss (Figure S7B).

The resistance penalty due to narrowing the ionic transport path through the integrated channel layer was minimal, due to the thin channel geometry and the relatively high conductivity of the cation-conducting layer. At industrially relevant currents (e.g., >100 mA cm^{-2}), we calculated the voltage drop within the integrated channel layer and the cation-conducting layer to be <1% and <10% of the full cell voltage, respectively (Figure 2D; supplemental information section 6). To verify the voltage drop of the integrated channel layer, we operated the electrolyzer using the same materials without integrated channels and found the cell voltages to be indistinguishable within measurement error, further confirming that the CO_2 capture channels do not present a significant resistive penalty (Figure S8D). However, without integrated capture channels, CO_2 formed at the junction of the cation and anion-conducting layers could not escape (Figure S8A). This trapped CO_2 caused the solid electrolyte to delaminate, resulting in <1 h of stable operation (Figures S8B and S8C), consistent with other literature reports using forward-bias bipolar configurations.[26–28,46] Using solid-state electrolyte packed beds[29–33] between the ion-conducting solid electrolyte layers allows CO_2 to escape (Figure S9A), but higher cell voltages (e.g., ∼700 mV, or ∼20%, more at 200 mA cm^{-2}) were required due to higher electrolyte and interfacial losses in the cell (Figure S9B). The integrated channel layer enables the effective removal of CO_2 without stability or cell voltage penalty.

Fixed cations to prevent salt precipitation

We sought an alkali-metal-free approach to prevent the third primary form of CO_2 loss: salt precipitation. We recognized that in zero-gap systems, alkali metal cations in the anolyte can migrate through the anion-conducting solid electrolyte to the cathode—as evidenced by poor CO_2RR performance when alkali metal cations are added in the anolyte (Figure S10).[21] We instead modulated the cathodic catalyst surface directly via a fixed cation in the poly(aryl piperidinium)[47] anion-conducting layer of the MSE (Figure 3A). The quaternary ammonium piperidinium cation has excellent stability in alkaline conditions and a high ionic conductivity of hydroxides and (bi)carbonates.[44,47–49] Operating without alkali metal cations, the selectivity toward CO_2RR products using the MSE was maintained above 80% in the range of 40–240 mA cm^{-2}, reaching a maximum of 95% (Figure 3B; Table S3). The low H_2 FE demonstrates that the cathodic environment, modulated by the piperidinium cation, was sufficiently alkaline to suppress H_2 production. At low currents, carbon monoxide was the dominant product (60% at 40 mA cm^{-2}). Selectivities toward C_2H_4 and ethanol increased with current and at 200 mA cm^{-2} reached 35% and 21%, respectively (Figure 3B). To assess the validity of our alkali-metal-free claim, we performed a control test with a pure water anolyte. The selectivity was

Please cite this article in press as: Xu et al., A microchanneled solid electrolyte for carbon-efficient CO_2 electrolysis, Joule (2022), https://doi.org/10.1016/j.joule.2022.04.023

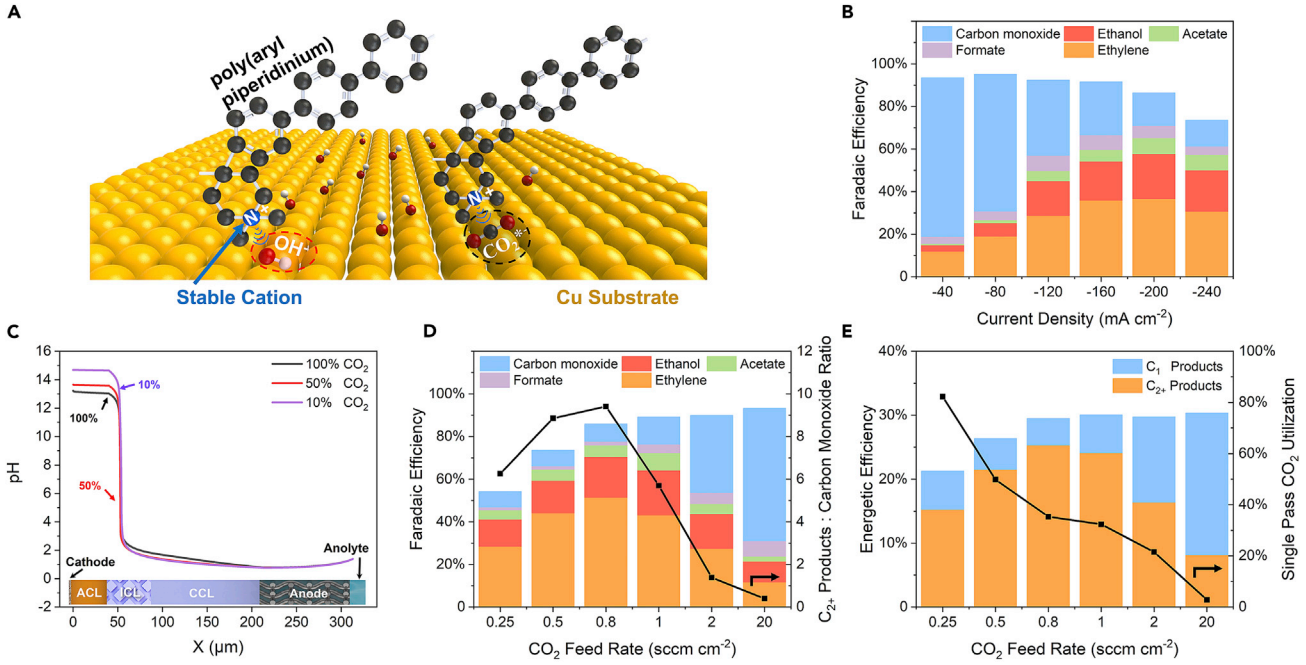

Figure 3. CO_2RR performance using microchanneled solid electrolyte for internal CO_2 regeneration (0.01 M H_2SO_4 anolyte)

(A) Schematic of poly(aryl piperidinium) functional group from the anion-conducting layer promoting CO_2RR.

(B) FE of major CO_2RR products at different current densities with a CO_2 feed rate of 20 sccm cm^{-2}.

(C) COMSOL simulation showing the pH distribution at different dissolved CO_2 content (100% is the ambient CO_2 solubility limit).

(D and E) (D) FE of major CO_2RR products and the ratio of C_{2+} products to carbon monoxide at different CO_2 feed rates, and (E) EE of C_1 and C_{2+} products and single-pass CO_2 utilization at different CO_2 feed rates.

The COMSOL simulation in (C) and the experiments in (D) and (E) were all performed at 100 mA cm^{-2}. The error of measurements indicated in Tables S3 and S5.

comparable with the case of 0.01 M sulfuric acid (H_2SO_4) anolyte (Figure S11). Analysis of the MSE outlet and anolyte outlet streams further confirmed a lack of alkali metal cations present (<2 ppm, Table S4). Alternative fixed cations provided by other anion-conducting layers, also resulted in successful CO_2RR without alkali metal cations (Figure S12). We recycled CO_2 captured from the integrated channel layer back to the cathode inlet during all experiments. Due to the high purity of the captured CO_2, there was no observable performance difference when the internally regenerated CO_2 stream was recycled, compared with an exclusively fresh CO_2 stream (Figure S13).

The rate-determining step for C_{2+} production,[50,51] C–C coupling, can be achieved at lower overpotentials in highly alkaline conditions.[6,52] We recognized that lowering the CO_2 concentration could lessen (bi)carbonate formation and increase the local pH. Our simulations indicated that lowering the CO_2 concentration from 100% to 10% would increase the cathode pH by 1.3 to ~14.7—the pH equivalent of 5 M potassium hydroxide (Figures 3C, S14, and S15). Beyond pH effects, previous reports suggest that lower partial pressures of CO_2 (or CO) reactant yield favorable reaction kinetics.[53,54] We reduced the CO_2 supply to the reactor, enabling a greater fraction of CO_2 to be consumed and greater dilution of CO_2 with gas products (all while recirculating internally regenerated CO_2). Decreasing the flow rate resulted in a substantial increase in C_2H_4 production at the expense of carbon monoxide, from a C_2H_4 selectivity of 12% at 20 sccm cm^{-2} to 51% at 0.8 sccm cm^{-2} (Figure 3D; Table S5). Decreasing the flow rate further increased H_2 selectivity due to CO_2 mass

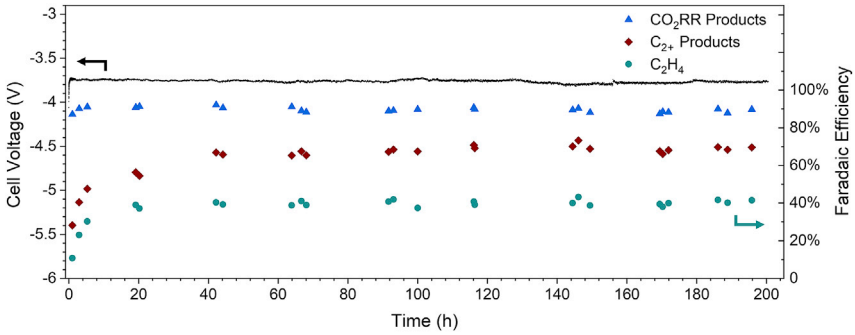

Figure 4. CO_2RR stability using microchanneled solid electrolyte for internal CO_2 regeneration (0.01 M H_2SO_4 anolyte, 100 mA cm^{-2}, and 1 sccm cm^{-2} CO_2 feed rate into the electrolyzer)
The CO_2 consumption rate for these conditions is quantified in Figure S19.

transport limitations. Single-pass CO_2 utilization, calculated using the fraction of the incoming CO_2 supply that is converted to CO_2RR products, increased monotonically with decreasing flow rate, up to 83% at 0.25 sccm cm^{-2} and 100 mA cm^{-2} (Figure 3E). The highest C_{2+} EEs of ~27% were obtained at 0.8 and 1.0 sccm cm^{-2}, but operation at 1.0 sccm cm^{-2} yielded less H_2 and a higher CO_2RR EE (Figure 3E).

Pilot-scale MSE performance

To demonstrate the scalability of our MSE design, we performed experiments in a custom pilot-scale cell having an active area of 50 cm^2 (Figure S16). For these experiments, the cathode substrate was changed from polytetrafluoroethylene (PTFE) to carbon paper (Sigracet 39 BB) to achieve through-plane electrode conductivity and minimize ohmic drop. The 50 cm^2 electrolyzer with the MSE exhibited slightly lower cell voltages and similar product selectivity as the smaller electrolyzer (Figure S17). Screening different flow rates for the 50 cm^2 yielded a maximum C_{2+} EE of 27% at 0.8 sccm cm^{-2}, the same flow rate as the smaller electrolyzer when both were operated at 100 mA cm^{-2} (Figure S18). If the electrolyzer were to operate at a larger current density, the CO_2 supply would have to be increased proportionally to ensure consistent electrochemical performance.[55,56] We quantified the CO_2 loss at the different CO_2 feed rates for the 50 cm^2 and demonstrated that the anodic CO_2 loss was <5% in all cases (Figure S18).

MSE stability

To demonstrate the stability of the electrolyzer with the MSE, we performed electrolysis galvanostatically at 100 mA cm^{-2} at a feed rate of 1 sccm cm^{-2} (Figure 4). Operating at this current density and flow rate limits CO_2 loss to ~3% (Figure S19). After an initial break-in period of 10 h, the FE toward C_2H_4 and all CO_2RR products remained constant for another 190 h at ~43% and >91%, respectively, with no indications of reduced performance at the end of the test period. While achieving minimal CO_2 loss, this work demonstrates the longest operating CO_2-to-C_{2+} electrolyzer at industrially relevant current densities (Table S6).

Conclusions

Overall, this work presents a strategy to minimize reactant CO_2 loss via an MSE, enabling net carbon-efficient CO_2 electrolysis. We implemented this strategy using CO_2 regeneration channels integrated within a solid electrolyte and poly(aryl piperidinium) as a fixed cation. Using this strategy, we achieved a C_2H_4 FE of 51% and a C_{2+} EE of 27%. This electrolyzer can also operate for 200 h of stable operation while maintaining ~3% CO_2 loss. With the achievement of these performance metrics, this

Please cite this article in press as: Xu et al., A microchanneled solid electrolyte for carbon-efficient CO_2 electrolysis, Joule (2022), https://doi.org/10.1016/j.joule.2022.04.023

strategy removes significant barriers to the commercial adoption of CO_2RR, enabling CO_2 mitigation and the storage of renewable energy in the form of carbon-based products.

EXPERIMENTAL PROCEDURES

Resource availability

Lead contact

Further information and requests for resources should be directed to and will be fulfilled by the lead contact, David Sinton (sinton@mie.utoronto.ca).

Materials availability

This study did not generate new unique reagents.

Data and code availability

The data presented in this work are available from the corresponding authors upon reasonable request.

Electrode preparation

The PTFE based copper electrode used was prepared by plasma sputtering. Approximately 300 nm of copper catalyst was sputtered onto the PTFE substrate using an AJA International ATC Orion 5 Sputter Deposition System (Toronto Nanofabrication Centre, Canada). The anode electrode was prepared by spray-coating iridium chloride on platinized titanium felt (Fuel Cell Store, USA) followed by thermal decomposition. An 8 × 8 cm^2 area of titanium felt was etched in boiling 0.5 M oxalic acid for 30 min. The etched titanium felt was then spray coated on a hot plate held at 80°C with a solution consisting of 200 mg $IrCl_3 \cdot xH_2O$ (99.8%, Alfa Aesar, USA) dissolved in 13 mL of ethanol. The titanium felt coated with $IrCl_3$ was then calcinated at 500°C for 10 min and cut to size to obtain the final anode electrode.

MSE preparation

The fabrication of the cation exchange membrane with internal microfluidic channels was performed as shown in Figure S20. The master for the microfluidic channels was prepared by spin-coating positive photoresist SU-8 2050 (Microchem, USA) with a height of 50 $\pm$ 5 μm on a silicon wafer.[57] The master was patterned with designed high-resolution transparency masks (CAD/Art Services, Inc., USA) following standard photolithography procedures.[58,59] The cation exchange membrane, Nafion 117 (Fuel Cell Store, USA), was hot embossed with the prepared master molds under a temperature of 220°F and pressure of 1.25 MPa for 5 min. The membrane was then soaked in a 3 wt % hydrogen peroxide (H_2O_2) solution at 80°C for 60 min to remove any impurities. Then, the membrane was soaked in 1 M H_2SO_4 at 80°C for 60 min for activation. After each of the H_2O_2 and H_2SO_4 immersion steps, the membrane was soaked in deionized water (18 MΩ cm^{-1}) at 80°C for 60 min to remove residual H_2O_2 and H_2SO_4. PiperION (PiperION TP-85, 40 μm, Versogen, USA), Sustainion (Sustainion X37-50 Grade RT, Dioxide Materials, USA), and Aemion (AF1-HNN8-50-X, Ionomr Innovations, Canada) anion exchange membranes were used. Anion exchange membranes were soaked in 1 M potassium hydroxide for 5 h at room temperature for activation, and then rinsed three times with deionized water to remove residual potassium hydroxide.

Electrochemical reduction of CO_2

All CO_2RR experiments were performed using an electrolyzer with an active area of 1 cm^2 at room temperature (~20°C) (Figures S21 and S22). During a CO_2RR experiment, the aqueous 0.01 M H_2SO_4 anolyte was circulated through the anode

flow channel at a flow rate of 25 mL min^{-1} using a peristaltic pump. The CO_2 gas flow was bubbled through water at room temperature for humidification prior to entering the electrolyzer. All voltages reported are full cell voltages without *i*R compensation.

Product analysis

The CO_2RR gas products were analyzed in 1 mL volumes using a gas chromatograph (PerkinElmer Clarus 590) equipped with a thermal conductivity detector (TCD) and a flame ionization detector (FID). The liquid products were quantified using ^{1}H nuclear magnetic resonance spectroscopy (NMR) on an Agilent DD2 500 spectrometer with dimethyl sulfoxide (DMSO) as an internal standard. For the stability tests, the electrolyzer was run uninterrupted with a fixed current density. The gas and liquid products were sampled periodically. Deionized water was added periodically to the electrolyte to compensate for water dragged through the cation-conducting layer. The products were manually collected periodically for analysis. The FE of CO_2RR gas products was calculated using the following equation:

$$FE_{gas} = x_i \times v \times \frac{z_i F P_o}{RT} \times \frac{1}{I_{total}} \times 100\%$$

where x_i is the volume fraction of gas product i; v is the outlet gas flow rate in sccm; z_i is the number of electrons required to produce one molecule of product I; F is the Faraday constant; P_0 is atmosphere pressure; R is the ideal gas constant; T is the temperature; and I_{total} is the total current.

The FE of CO_2RR liquid products was calculated using the following equation:

$$FE_{liquid} = n_i \times \frac{z_i F}{Q} \times 100\%$$

where n_i is the number of moles of liquid product i, and Q is the cumulative charge as the liquid products were collected.

The EE of CO_2RR products was calculated using the following equation:

$$EE_i = \frac{E_i^{\circ}}{E_{cell}} \times FE_i$$

where E_i° is the thermodynamic potential for each product,[50] and E_{cell} is the applied cell voltage without *i*R compensation.

SUPPLEMENTAL INFORMATION

Supplemental information can be found online at https://doi.org/10.1016/j.joule.2022.04.023.

ACKNOWLEDGMENTS

The authors acknowledge support from the Natural Sciences and Engineering Research Council (NSERC) of Canada and Natural Resources Canada—Clean Growth Program. Support from Canada Research Chairs Program is gratefully acknowledged, as is support from an NSERC E.W.R. Steacie Fellowship to D.S. Y.X. acknowledges NSERC for their support through graduate scholarships. J.P.E. thanks NSERC, Hatch, and the Government of Ontario for their support through graduate scholarships.

AUTHOR CONTRIBUTIONS

D.S. and E.H.S. supervised the project. Y.X., R.K.M., and J.P.E. designed experiments and analyzed results. Y.X. and R.K.M. carried out all the experiments. Y.X.

and J.P.E. drafted the manuscript. S.L. performed COMSOL simulations. C.P.O. and C.M.G. performed large-scale experiments. Y.X., R.K.M., and M.F. synthesized catalysts. J.E.H. and A.R. performed product analysis. All authors discussed the results and assisted during manuscript preparation.

DECLARATION OF INTERESTS

The authors declare the following competing financial interest(s): there is a patent application pending, filed by the authors of this Letter and their institutions.

Received: September 29, 2021
Revised: January 4, 2022
Accepted: April 26, 2022
Published: May 25, 2022

REFERENCES

1. He, J., and Janáky, C. (2020). Recent advances in solar-driven carbon dioxide conversion: expectations versus reality. ACS Energy Lett. *5*, 1996–2014.
2. Masel, R.I., Liu, Z., Yang, H., Kaczur, J.J., Carrillo, D., Ren, S., Salvatore, D., and Berlinguette, C.P. (2021). An industrial perspective on catalysts for low-temperature CO_2 electrolysis. Nat. Nanotechnol. *16*, 118–128.
3. Kenis, P.J.A., Dibenedetto, A., and Zhang, T. (2017). Carbon dioxide utilization coming of age. ChemPhysChem *18*, 3091–3093.
4. Chen, X., Chen, J., Alghoraibi, N.M., Henckel, D.A., Zhang, R., Nwabara, U.O., Madsen, K.E., Kenis, P.J.A., Zimmerman, S.C., and Gewirth, A.A. (2021). Electrochemical CO_2-to-ethylene conversion on polyamine-incorporated Cu electrodes. Nat. Cat *4*, 20–27.
5. Ma, W., Xie, S., Liu, T., Fan, Q., Ye, J., Sun, F., Jiang, Z., Zhang, Q., Cheng, J., and Wang, Y. (2020). Electrocatalytic reduction of CO_2 to ethylene and ethanol through hydrogen-assisted C–C coupling over fluorine-modified copper. Nat. Cat. *3*, 478–487.
6. Dinh, C.T., Burdyny, T., Kibria, M.G., Seifitokaldani, A., Gabardo, C.M., García de Arquer, F.P., Kiani, A., Edwards, J.P., De Luna, P., Bushuyev, O.S., et al. (2018). CO_2 electroreduction to ethylene via hydroxide-mediated copper catalysis at an abrupt interface. Science *360*, 783–787.
7. Gabardo, C.M., O'Brien, C.P., Edwards, J.P., McCallum, C., Xu, Y., Dinh, C.-T., Li, J., Sargent, E.H., and Sinton, D. (2019). Continuous carbon dioxide electroreduction to concentrated multi-carbon products using a membrane electrode assembly. Joule *3*, 2777–2791.
8. Li, F., Thevenon, A., Rosas-Hernández, A., Wang, Z., Li, Y., Gabardo, C.M., Ozden, A., Dinh, C.T., Li, J., Wang, Y., et al. (2020). Molecular tuning of CO_2-to-ethylene conversion. Nature *577*, 509–513.
9. Ozden, A., Li, F., García de Arquer, F.P., Rosas-Hernández, A., Thevenon, A., Wang, Y., Hung, S.-F., Wang, X., Chen, B., Li, J., et al. (2020). High-rate and efficient ethylene electrosynthesis using a catalyst/promoter/transport layer. ACS Energy Lett. *5*, 2811–2818.
10. Zhong, M., Tran, K., Min, Y., Wang, C., Wang, Z., Dinh, C.-T., De Luna, P., Yu, Z., Rasouli, A.S., Brodersen, P., et al. (2020). Accelerated discovery of CO_2 electrocatalysts using active machine learning. Nature *581*, 178–183.
11. Burdyny, T., and Smith, W.A. (2019). CO_2 reduction on gas-diffusion electrodes and why catalytic performance must be assessed at commercially-relevant conditions. Energy Environ. Sci. *12*, 1442–1453.
12. McCallum, C., Gabardo, C.M., O'Brien, C.P., Edwards, J.P., Wicks, J., Xu, Y., Sargent, E.H., and Sinton, D. (2021). Reducing the crossover of carbonate and liquid products during carbon dioxide electroreduction. Cell Rep. Phys. Sci. *2*, 100522.
13. Sisler, J., Khan, S., Ip, A.H., Schreiber, M.W., Jaffer, S.A., Bobicki, E.R., Dinh, C.-T., and Sargent, E.H. (2021). Ethylene electrosynthesis: a comparative techno-economic analysis of alkaline vs membrane electrode assembly vs CO_2–CO–C_2H_4 tandems. ACS Energy Lett. *6*, 997–1002.
14. Ozden, A., Wang, Y., Li, F., Luo, M., Sisler, J., Thevenon, A., Rosas-Hernández, A., Burdyny, T., Lum, Y., Yadegari, H., et al. (2021). Cascade CO_2 electroreduction enables efficient carbonate-free production of ethylene. Joule *5*, 706–719.
15. Rabinowitz, J.A., and Kanan, M.W. (2020). The future of low-temperature carbon dioxide electrolysis depends on solving one basic problem. Nat. Commun. *11*, 5231.
16. Ma, M., Clark, E.L., Therkildsen, K.T., Dalsgaard, S., Chorkendorff, I., and Seger, B. (2020). Insights into the carbon balance for CO_2 electroreduction on Cu using gas diffusion electrode reactor designs. Energy Environ. Sci. *13*, 977–985.
17. Ma, M., Kim, S., Chorkendorff, I., and Seger, B. (2020). Role of ion-selective membranes in the carbon balance for CO_2 electroreduction *via* gas diffusion electrode reactor designs. Chem. Sci. *11*, 8854–8861.
18. Larrazábal, G.O., Strøm-Hansen, P., Heli, J.P., Zeiter, K., Therkildsen, K.T., Chorkendorff, I., and Seger, B. (2019). Analysis of mass flows and membrane cross-over in CO_2 reduction at high current densities in an MEA-type electrolyzer. ACS Appl. Mater. Interfaces *11*, 41281–41288.
19. Cofell, E.R., Nwabara, U.O., Bhargava, S.S., Henckel, D.E., and Kenis, P.J.A. (2021). Investigation of electrolyte-dependent carbonate formation on gas diffusion electrodes for CO_2 electrolysis. ACS Appl. Mater. Interfaces *13*, 15132–15142.
20. Xu, Y., Edwards, J.P., Liu, S., Miao, R.K., Huang, J.E., Gabardo, C.M., O'Brien, C.P., Li, J., Sargent, E.H., and Sinton, D. (2021). Self-cleaning CO_2 reduction systems: unsteady electrochemical forcing enables stability. ACS Energy Lett. *6*, 809–815.
21. Endrődi, B., Samu, A., Kecsenovity, E., Halmágyi, T., Sebők, D., and Janáky, C. (2021). Operando cathode activation with alkali metal cations for high current density operation of water-fed zero-gap carbon dioxide electrolysers. Nat. Energy *6*, 439–448.
22. Overa, S., Feric, T.G., Park, A.-H.A., and Jiao, F. (2021). Tandem and hybrid processes for carbon dioxide utilization. Joule *5*, 8–13.
23. Endrődi, B., Kecsenovity, E., Samu, A., Darvas, F., Jones, R.V., Török, V., Danyi, A., and Janáky, C. (2019). Multilayer electrolyzer stack converts carbon dioxide to gas products at high pressure with high efficiency. ACS Energy Lett. *4*, 1770–1777.
24. Nwabara, U.O., Hernandez, A.D., Henckel, D.A., Chen, X., Cofell, E.R., de-Heer, M.P., Verma, S., Gewirth, A.A., and Kenis, P.J.A. (2021). Binder-focused approaches to improve the stability of cathodes for CO_2 electroreduction. ACS Appl. Energy Mater. *4*, 5175–5186.
25. Verma, S., Hamasaki, Y., Kim, C., Huang, W., Lu, S., Jhong, H.-R.M., Gewirth, A.A., Fujigaya, T., Nakashima, N., and Kenis, P.J.A. (2018). Insights into the low overpotential electroreduction of CO_2 to CO on a supported gold catalyst in an alkaline flow electrolyzer. ACS Energy Lett. *3*, 193–198.
26. Blommaert, M.A., Sharifian, R., Shah, N.U., Nesbitt, N.T., Smith, W.A., and Vermaas, D.A. (2021). Orientation of bipolar membrane determines the dominant ion and carbonic species transport in membrane electrode assemblies for CO_2 reduction. J. Mater. Chem. A Mater. *9*, 11179–11186.

27. Pătru, A., Binninger, T., Pribyl, B., and Schmidt, T.J. (2019). Design principles of bipolar electrochemical co-electrolysis cells for efficient reduction of carbon dioxide from gas phase at low temperature. J. Electrochem. Soc. *166*, F34–F43.

28. Pribyl-Kranewitter, B., Beard, A., Schuler, T., Diklić, N., and Schmidt, T.J. (2021). Investigation and optimisation of operating conditions for low-temperature CO_2 reduction to CO in a forward-bias bipolar-membrane electrolyser. J. Electrochem. Soc. *168*, 043506.

29. Xia, C., Zhu, P., Jiang, Q., Pan, Y., Liang, W., Stavitski, E., Alshareef, H.N., and Wang, H. (2019). Continuous production of pure liquid fuel solutions via electrocatalytic CO_2 reduction using solid-electrolyte devices. Nat. Energy *4*, 776–785.

30. Liu, Z., Masel, R.I., Chen, Q., Kutz, R., Yang, H., Lewinski, K., Kaplun, M., Luopa, S., and Lutz, D.R. (2016). Electrochemical generation of syngas from water and carbon dioxide at industrially important rates. J. CO_2 Util. *15*, 50–56.

31. Fan, L., Xia, C., Zhu, P., Lu, Y., and Wang, H. (2020). Electrochemical CO_2 reduction to high-concentration pure formic acid solutions in an all-solid-state reactor. Nat. Commun. *11*, 3633.

32. Miao, R.K., Xu, Y., Ozden, A., Robb, A., O'Brien, C.P., Gabardo, C.M., Lee, G., Edwards, J.P., Huang, J.E., Fan, M., et al. (2021). Electroosmotic flow steers neutral products and enables concentrated ethanol electroproduction from CO_2. Joule *5*, 2742–2753.

33. Kaczur, J.J., McGlaughlin, L.J., and Lakkaraju, P.S. (2020). Investigating pervaporation as a process method for concentrating formic acid produced from carbon dioxide. J. Carbon Res. *6*, 42.

34. Huang, J.E., Li, F., Ozden, A., Sedighian Rasouli, A., García de Arquer, F.P., Liu, S., Zhang, S., Luo, M., Wang, X., Lum, Y., et al. (2021). CO_2 electrolysis to multicarbon products in strong acid. Science *372*, 1074–1078.

35. Alerte, T., Edwards, J.P., Gabardo, C.M., O'Brien, C.P., Gaona, A., Wicks, J., Obradović, A., Sarkar, A., Jaffer, S.A., MacLean, H.L., et al. (2021). Downstream of the CO_2 electrolyzer: assessing the energy intensity of product separation. ACS Energy Lett. *6*, 4405–4412.

36. Sharifian, R., Wagterveld, R.M., Digdaya, I.A., Xiang, C., and Vermaas, D.A. (2021). Electrochemical carbon dioxide capture to close the carbon cycle. Energy Environ. Sci. *14*, 781–814.

37. Salvatore, D.A., Gabardo, C.M., Reyes, A., O'Brien, C.P., Holdcroft, S., Pintauro, P., Bahar, B., Hickner, M., Bae, C., Sinton, D., et al. (2021). Designing anion exchange membranes for CO_2 electrolysers. Nat. Energy *6*, 339–348.

38. Barber, J. (2007). Biological solar energy. Philos. Trans. A Math. Phys. Eng. Sci. *365*, 1007–1023.

39. Brodribb, T.J., Feild, T.S., and Sack, L. (2010). Viewing leaf structure and evolution from a hydraulic perspective. Funct. Plant Biol. *37*, 488.

40. Parkhurst, D.F. (1994). Diffusion of CO_2 and other gases inside leaves. New Phytol. *126*, 449–479.

41. Tian, Y.L., Zhao, Y.C., Yang, C.J., Wang, F.J., Liu, X.P., and Jing, X.B. (2018). Fabrication of bio-inspired nitinol alloy surface with tunable anisotropic wetting and high adhesive ability. J. Colloid Interface Sci. *527*, 328–338.

42. Xu, H., Li, H., and Chang, J. (2013). Controlled drug release from a polymer matrix by patterned electrospun nanofibers with controllable hydrophobicity. J. Mater. Chem. B *1*, 4182–4188.

43. De Pra, M., De Malsche, W., Desmet, G., Schoenmakers, P.J., and Kok, W.Th. (2007). Pillar-structured microchannels for on-chip liquid chromatography: evaluation of the permeability and separation performance. J. Sep. Sci. *30*, 1453–1460.

44. Endrődi, B., Kecsenovity, E., Samu, A., Halmágyi, T., Rojas-Carbonell, S., Wang, L., Yan, Y., and Janáky, C. (2020). High carbonate ion conductance of a robust PiperION membrane allows industrial current density and conversion in a zero-gap carbon dioxide electrolyzer cell. Energy Environ. Sci. *13*, 4098–4105.

45. Zheng, T., Jiang, K., Ta, N., Hu, Y., Zeng, J., Liu, J., and Wang, H. (2019). Large-scale and highly selective CO_2 electrocatalytic reduction on nickel single-atom catalyst. Joule *3*, 265–278.

46. O'Brien, C.P., Miao, R.K., Liu, S., Xu, Y., Lee, G., Robb, A., Huang, J.E., Xie, K., Bertens, K., Gabardo, C.M., et al. (2021). Single pass CO_2 conversion exceeding 85% in the electrosynthesis of multicarbon products via local CO_2 regeneration. ACS Energy Lett. 2952–2959.

47. Wang, J., Zhao, Y., Setzler, B.P., Rojas-Carbonell, S., Ben Yehuda, C., Amel, A., Page, M., Wang, L., Hu, K., Shi, L., et al. (2019). Poly(aryl piperidinium) membranes and ionomers for hydroxide exchange membrane fuel cells. Nat. Energy *4*, 392–398.

48. Luo, X., Rojas-Carbonell, S., Yan, Y., and Kusoglu, A. (2020). Structure-transport relationships of poly(aryl piperidinium) anion-exchange membranes: Eeffect of anions and hydration. J. Membr. Sci. *598*, 117680.

49. Marino, M.G., and Kreuer, K.D. (2015). Alkaline stability of quaternary ammonium cations for alkaline fuel cell membranes and ionic liquids. ChemSusChem *8*, 513–523.

50. Nitopi, S., Bertheussen, E., Scott, S.B., Liu, X., Engstfeld, A.K., Horch, S., Seger, B., Stephens, I.E.L., Chan, K., Hahn, C., et al. (2019). Progress and perspectives of electrochemical CO_2 reduction on copper in aqueous electrolyte. Chem. Rev. *119*, 7610–7672.

51. Montoya, J.H., Peterson, A.A., and Nørskov, J.K. (2013). Insights into C–C coupling in CO_2 electroreduction on copper electrodes. ChemCatChem *5*, 737–742.

52. Liu, X., Schlexer, P., Xiao, J., Ji, Y., Wang, L., Sandberg, R.B., Tang, M., Brown, K.S., Peng, H., Ringe, S., et al. (2019). pH effects on the electrochemical reduction of CO(2) towards C2 products on stepped copper. Nat. Commun. *10*, 32.

53. Li, J., Wang, Z., McCallum, C., Xu, Y., Li, F., Wang, Y., Gabardo, C.M., Dinh, C.-T., Zhuang, T.-T., Wang, L., et al. (2019). Constraining CO coverage on copper promotes high-efficiency ethylene electroproduction. Nat. Cat. *2*, 1124–1131.

54. Tan, Y.C., Lee, K.B., Song, H., and Oh, J. (2020). Modulating local CO_2 concentration as a general strategy for enhancing C−C coupling in CO_2 electroreduction. Joule *4*, 1104–1120.

55. Jeanty, P., Scherer, C., Magori, E., Wiesner-Fleischer, K., Hinrichsen, O., and Fleischer, M. (2018). Upscaling and continuous operation of electrochemical CO_2 to CO conversion in aqueous solutions on silver gas diffusion electrodes. J. CO_2 Util. *24*, 454–462.

56. Krause, R., Reinisch, D., Reller, C., Eckert, H., Hartmann, D., Taroata, D., Wiesner-Fleischer, K., Bulan, A., Lueken, A., and Schmid, G. (2020). Industrial application aspects of the electrochemical reduction of CO_2 to CO in aqueous electrolyte. Chem. Ing. Tech. *92*, 53–61.

57. Wang, P.Y., and Mason, T.G. (2018). A Brownian quasi-crystal of pre-assembled colloidal Penrose tiles. Nature *561*, 94–99.

58. Kim, E., Xia, Y., and Whitesides, G.M. (1995). Polymer microstructures formed by moulding in capillaries. Nature *376*, 581–584.

59. Chowdhury, M.S., Zheng, W., Kumari, S., Heyman, J., Zhang, X., Dey, P., Weitz, D.A., and Haag, R. (2019). Dendronized fluorosurfactant for highly stable water-in-fluorinated oil emulsions with minimal inter-droplet transfer of small molecules. Nat. Commun. *10*, 4546.